actuators

Article

Experimental Investigation on the Combined Blowing Control of a Hybrid Wing Body Aircraft

Jiaxin Pan, Wanbo Wang *, Chen Qin, Xunnian Wang, Qixiang Sun and Xin Zhang

State Key Laboratory of Aerodynamics, China Aerodynamics Research and Development Center,
Mianyang 621000, China; bc22005009@mail.ustc.edu.cn (J.P.)
* Correspondence: bowanw@163.com

Abstract: Combined blowing was performed on a Hybrid Wing Body (HWB) aircraft through wind tunnel testing at a Reynolds number of 1.75×10^6. The full cycle of separation and reattachment under the control of combined blowing was implemented using Computational Fluid Dynamics (CFD), and the mechanism of combined blowing inhibiting separation was analyzed. The aerodynamic characteristics of the baseline and the independent effects of the blown deflected trailing edge (TE), blown leading edge (LE), and combined blowing on the TE and LE were investigated. The results clearly show that combined blowing can inhibit the development of cross-flow, reduce the accumulation of a boundary layer at the tip, and inhibit the flow separation effect. The effect of using seamless simple flaps alone to increase the lift is limited; blowing control is required to enhance the lift further. Applying the blown deflected TE can improve the lift linear segment, so that 30° flap achieves the lift gain of 40° flap without control, while the drag coefficient is approximately 0.02 smaller, but the stall gradually advances. Using the blown LE can significantly increase the stall angle from 12° to 18°. However, the lift linear segment remains unaffected. In particular, combined blowing can achieve the control effect of improving the lift linear segment, delaying stall, and decreasing drag. Moreover, the maximum lift coefficient is approximately 0.19, and the lift-to-drag ratio increment in the control state with a 30° flap deflection angle is above 2.2 in the angle of attack range of 4° to 12° compared to the uncontrolled state with a 40° flap deflection angle.

Keywords: Hybrid Wing Body; wind tunnel force test; lift enhancement; blowing flow control

Citation: Pan, J.; Wang, W.; Qin, C.; Wang, X.; Sun, Q.; Zhang, X. Experimental Investigation on the Combined Blowing Control of a Hybrid Wing Body Aircraft. *Actuators* **2023**, *12*, 237. https://doi.org/10.3390/act12060237

Academic Editor: Luigi de Luca

Received: 17 May 2023
Revised: 4 June 2023
Accepted: 5 June 2023
Published: 8 June 2023

Copyright: © 2023 by the authors. Licensee MDPI, Basel, Switzerland. This article is an open access article distributed under the terms and conditions of the Creative Commons Attribution (CC BY) license (https://creativecommons.org/licenses/by/4.0/).

1. Introduction

Compared to conventional configurations, the Blended Wing Body (BWB) or Hybrid Wing Body (HWB) layout significantly reduces the wetted area. It has more significant advantages in terms of drag and noise reduction [1–6]. However, limited longitudinal control authority due to the short lever arm of the BWB layout is a critical challenge. This issue is usually solved by lengthening the body, adding a horizontal tail, or using active flow control [3]. The HWB layout developed by the Lock Martin (LM) company keeps the characteristics of the BWB, with a smooth transition between the wings and the body. The remaining part retains the longer cylindrical fuselage of the traditional layout and the "T-shaped" tail to enhance longitudinal control authority [7]. This design not only has the same load distribution advantages as the BWB, but the wing and fuselage transition section also helps to prevent sudden changes in inertial loads, and the rounded fuselage in the rear half supports the internal structural arrangement [1].

The LM-HWB configuration uses the same leading edge slats and Fowler flaps as conventional aircraft [8]. This conventional lift enhancement method requires complex working mechanisms for safe operation, usually covered by fairings and protruding under the wings, creating detrimental drag [9].

Seamless, simple flaps do not involve complex drive mechanisms, but the airflow on the flap surface is easily separated, resulting in limited lift. The concept of a seamless, simple flap based on blowing flow control, which can significantly suppress airflow separation, has been revived [10] and is receiving increasing attention in research [11–14]. Applying internal-blown flaps can significantly increase lift and cause earlier stalls [15]. Therefore, the deployed slat increases the stall angle, as in the case of the HWB STOL (Short Take-Off and Landing) model applied in the LaRC (Langley Research Center) subsonic wind tunnel by Collins et al. The model uses a combination of deployed slats and internal-blown flaps to achieve STOL [16]. The FAST-MAC (Fundamental Aerodynamics Subsonic/Transonic-Modular Active Control) wing-body-composite half-model low-speed high-lift configuration was tested in the NTF (National Transonic Facility) transonic wind tunnel by Milholen et al. using a 10%c deployed slat and an internal-blown flap [17]. In 2020, Lin et al. compared a simple flap lift solution based on a 10% scaled-down CRM (Common Research Model) wind tunnel test model using a combination of swept and constant blowing actuators with a conventional Fowler flap lift solution in the LaRC subsonic wind tunnel, showing that the latter was more efficient [18].

However, when LE slats are deployed, the concave pressure surface has a low-velocity reverse region. The free shear layer developing from the sharp lower TE collides with the slat TE pressure surface, affecting drag and noise during take-off and landing conditions [19]. Research has shown that the combination of LE blowing and internal-blown flaps can effectively increase the stall angle of attack and maximum lift coefficient and reduce the noise of the aircraft [15,20].

The HWB has been proven to have a good high-speed cruise performance [8,21,22], but there are many problems with the application of conventional lift devices to such aircraft with new layouts [7]. Combined blowing lift enhancement solutions can replace leading edge slats and Fuller flaps, but there is little research on the application of this technology to aircraft with new layouts. Based on existing blowing flow control research, this paper uses a half-mode model of an HWB layout with blowing slots on the leading and tailing edges of the main wing, exploring the combined blowing lift enhancement scheme for HWB through CFD methods and wind tunnel tests to investigate the flow characteristics and mechanism of action under blowing control, providing new insights and methods to improve the overall performance of the HWB layout.

2. Test Equipment and Method

2.1. Test Device

The blowing control methods include TE blowing, LE blowing, and combined blowing, as seen in Figure 1.

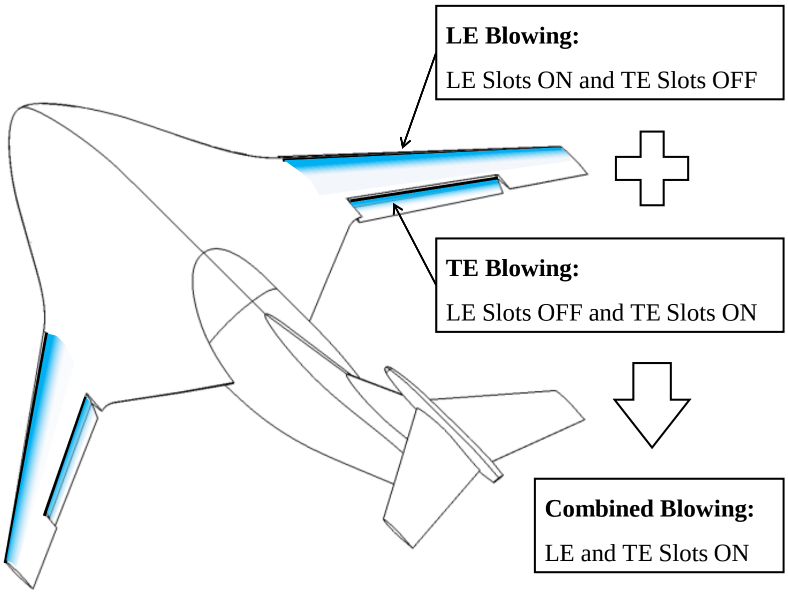

Figure 1. Diagram of the blowing control scheme.

The test was conducted in a recirculating low-speed wind tunnel at the China Aerodynamics Research and Development Center. The cross-section size of the test section was 1.8 m (width) × 1.4 m (height). The stable wind speed range was 10 m/s~105 m/s, the turbulence intensity reached 0.0008 when the wind speed was lower than 70 m/s, and the axial static pressure gradient was above 0.005.

The agent model was connected to a box-type balance below the test section floor through a support, as depicted in Figure 2a. The balance was fixed to the turntable below the wind tunnel with the balance support table. The variable lateral sliding angle mechanism of the lower turntable altered the angle of attack of the model. The wall boundary effect was mitigated by installing fairing pads. The pad height was 20 mm, the maze groove sealed the pad and the model to prevent the pad and the model from coming into contact and transmitting force, the maze groove clearance was 5 mm, and the pad was secured to the circular floor.

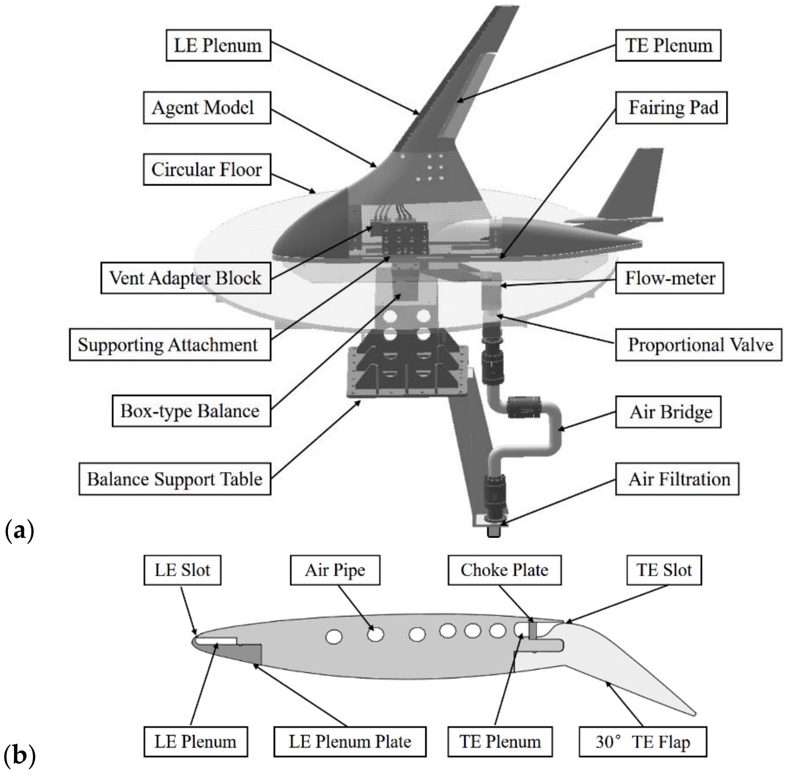

Figure 2. Schematic diagram of the test model: (**a**) general assembly; (**b**) wing internal profile.

2.2. Test Model

The test model was a half-model of an HWB aircraft, including the nose, fuselage, main wing, vertical tail, horizontal tail, and flap, with a half-span of 994 mm and an average aerodynamic chord of 512 mm. The flap was a seamless, simple flap; the flap chord length was approximately 33%c; the flap offset was set to 0°, 30°, 40°, and 60°; and each component was created through aluminum metal processing. Two blowing plenums were arranged in the wing, and blowing control was achieved by controlling the compressed air supply. The total length of the LE slot was 685 mm, being approximately 0.1 mm high; the total length of the TE slot was 377 mm, being approximately 0.4 mm high; and these blowing slots were locked with a span-to-array screw hole (spacing approximately 40 mm).

Based on the relevant research [23–25], it is known that the effect of blowing control near the point of flow separation is suitable. The LE and TE slots were set at 3%c and 63%c, respectively, from the LE, and these slots were typically tangent to the surface. The TE of the main wing was fixed with a hinge, and the TE slot was easily established at the position where the main wing and flap were connected [13]. This will be introduced into the Numerical Calculation section to determine the position of the LE slot.

2.3. Air Supply Device and Method

Before entering the model air supply pipeline, compressed air passes through air filtration, the air bridge, the proportional valve, and the high-precision flow meter, as shown in Figure 1. The air bridge mainly comprised two transverse flexible joints and one flexible vertical joint. The flexible vertical joint could absorb the expansion of the two transverse flexible joints. The two transverse flexible joints could also absorb the expansion of the flexible vertical joint, thus eliminating the influence of the supply pipe on the balance force measurement. Two proportional valves accurately controlled the flow rate of the main wing's leading and trailing edge jet; two high-precision flow meters measured the flow rate of blowing. The measurement accuracy was approximately 0.01 g/s.

Compressed air was connected to the model supply pipe via polyurethane pipes, and two closed four-way vent adapter blocks were fixed inside the model. Three supply pipes connected the LE and TE plenums to the two vent adapter blocks. The flap was connected to the TE plenum through a row of screws arrayed in the span direction. The flow in each plenum passes through a choke plate to achieve a uniform flow along the span of the blown slot. Sealing strips and glue were used to seal the gap between the flaps and the wing, as seen in Figure 2b.

A photograph of the test model is shown in Figure 3, with the screw holes on the model's surface all filled in the test.

Figure 3. A front view of the test model.

The dimensionless momentum coefficient is expressed as the jet strength, as shown in Equation (1).

$$C_\mu = \frac{m_j U_j}{qS} = \frac{m_j}{qS}\left\{\frac{2\gamma R T_0}{\gamma - 1}\left[1 - \left(\frac{P_a}{P_0}\right)^{\frac{\gamma-1}{\gamma}}\right]\right\}^{\frac{1}{2}} \quad (1)$$

The mass flow rate m_j in the gas supply line is measured with the flow control unit, q is the test velocity pressure, S is the model reference area, and C_μ can be found for a given pressure ratio.

3. Numerical Calculation

3.1. Calculation Models and Methods

The position of the LE slot was determined via CFD, and we analyzed the combined blowing control mechanism. The calculation software is based on the NNW-FlowStar open-source fluid engineering software developed by the China Aerodynamic Research and Development Center (CARDC) [26]. The control equation is a three-dimensional viscous compressible unsteady Reynolds-averaged Navier–Stokes equation; thus, the control equation takes the following integral form:

$$\frac{\partial}{\partial t}\int\int\int Q\mathrm{d}V+\int\int f\cdot n\mathrm{d}S=0 \tag{2}$$

where t is a time quantity, V denotes the volume of the control body, S denotes the surface area of the control body, Q is a conserved variable, f is the sum of the inviscid and viscous fluxes through the surface S, and n is the outer normal unit vector of the control body surface S. The control equations were discretized using the finite volume method, with the fluxes in Roe [27] format numerically and in second-order backward differential format in time, the spatial discretization format being a second-order accuracy windward format, and the k-ω SST turbulence model was used to close the mean Reynolds equation. The dimensionless time step $\Delta t^* = \Delta t \times U/c = 0.002$, and the LU-SGS (Lower-Upper Symmetric Gauss–Seidel) implicit time advance algorithm was used. The calculation of the region entrance, exit, and upper and lower boundary distances of the aircraft was 40 times the chord length, and the first boundary layer grid thickness was approximately 1×10^{-5} m. The model surface mesh and the symmetrical surface part of the mesh are shown in Figure 4. The model surface satisfies the no-slip boundary condition, the jet boundary is the velocity inlet boundary, and the calculated angle of attack range is 0°~10°. Figure 5 shows the distribution of y+ on the wing surface mesh. In the figure, y+ is less than 5 for the mesh, and in most areas, y+ remains around 1, indicating a complete solution of the boundary layer. The size of the CFD model remains the same as that of the test model. The calculations use symmetrical surface boundary conditions and do not consider the boundary layer effects of the floor; thus, the fairing pad is not included in the CFD model. The far field has a velocity inlet set at 50 m/s, and the outlet boundary condition is set to a static pressure outlet, while all other boundary conditions in the far field are set to free-slip wall boundary conditions. The jet slots are all set to velocity inlet conditions, and the LE momentum coefficient and TE momentum coefficient are calculated to be 0.03 and 0.005, respectively. The numerical Reynolds number is consistent with the real wind tunnel test at approximately 1.75×10^6.

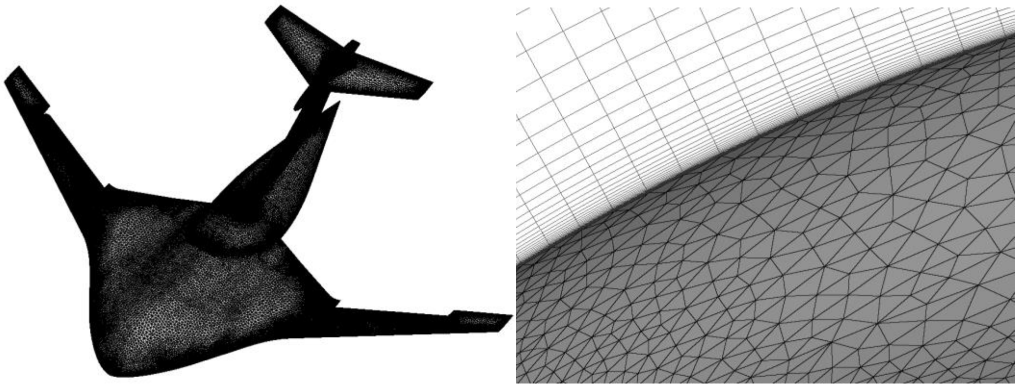

Figure 4. CFD mesh of the HWB model.

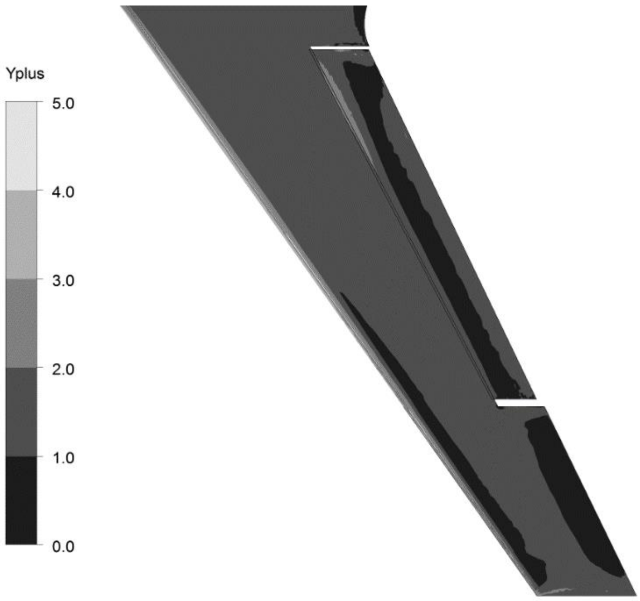

Figure 5. Wing surface grid y+ distribution.

3.2. Calculation Validation

To analyze the impact of the mesh size and ensure the independence of the grid configuration in regard to the calculation results, three grids of different densities were generated for the model cruise state and compared with the experimental data.

The error between the numerical simulations and experimental data gradually decreased as the grid size increased. The lift coefficients calculated with grid sizes of 5 million, 10 million, and 15 million had errors of 2.1%, 0.8%, and 0.6%, respectively, compared to the experimental results. As the medium-density grid closely approximated the denser grid and was in good agreement with the test results, we used a 10-million-number grid to improve the computational efficiency.

Figure 6 compares the wind tunnel test and CFD results at a wind speed of 50 m/s and Reynolds number of approximately 1.75 × 10^6. For the cruise and 30° flap state, the linear section lift results of the wind tunnel test and CFD are more consistent, indicating that the CFD results are reliable.

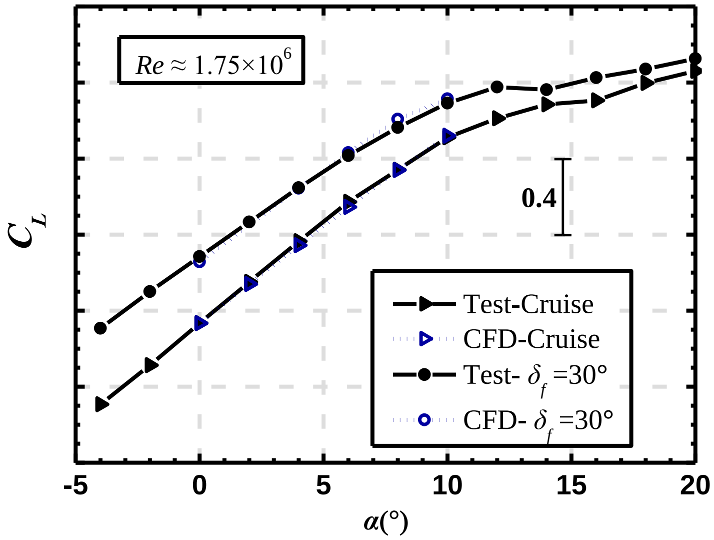

Figure 6. Comparison of wind tunnel test and CFD results.

3.3. Position of the LE Slot

The lift characteristics corresponding to different LE blowing positions obtained via CFD can be seen in Figure 7, where $C_{\mu l}$ and $C_{\mu t}$ are the momentum coefficients of LE and TE blowing, respectively.

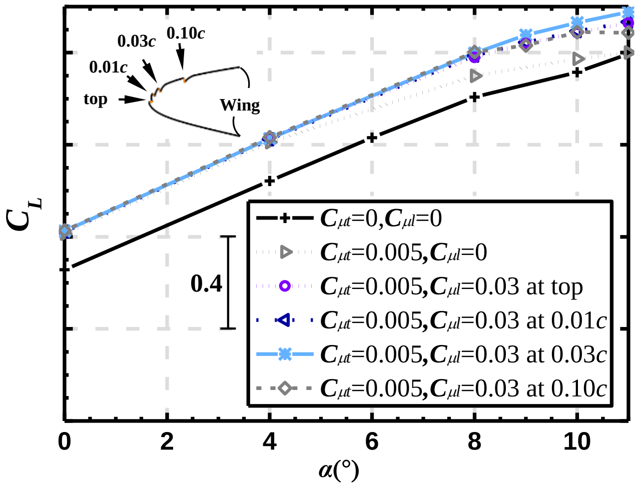

Figure 7. Lift coefficients at different LE jet positions.

It can be seen that when $\alpha \leq 8°$, the influence of different LE blowing positions on the lift coefficient is small. With the increasing angle of attack, the lift effect is better when the LE slot is at 3%c; thus, this location was chosen. Figure 8 presents the pitch moment coefficient results before and after combined blowing control. Compared to the uncontrolled state, combined blowing increases the nose-down moment by 48%, which is similar to the results obtained from the high-lift configuration used in the HWB described in [28]. The reason for this may be that the pitch moment center of gravity of the HWB layout is relatively forward, which inevitably leads to additional nose-down moments after increasing the lift. As the research on horizontal tailplane balancing is complex, with many influencing factors, it is not the focus of this study. Additionally, no elevator deflection was carried out during the research process. Therefore, this pitch moment coefficient result is only briefly explained in the calculation section of this paper.

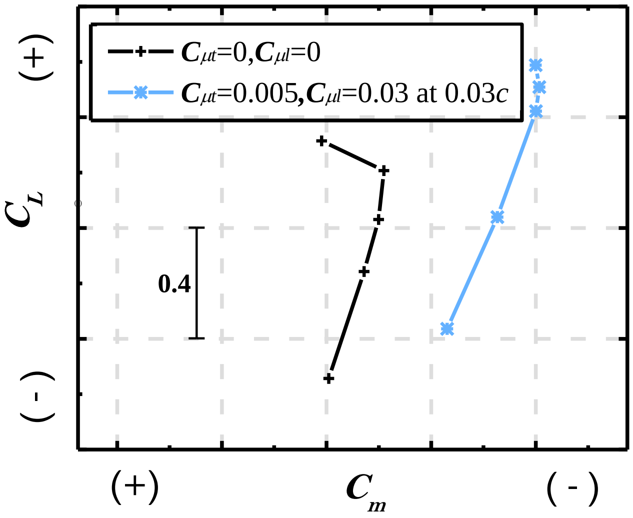

Figure 8. Pitching moment coefficients before and after combined blowing control.

3.4. Combinatorial Blowing Control Process

To analyze the combined blowing control process and understand the blowing control mechanism, the calculated results of the shear stresses and flow lines on the wing surface for different momentum coefficients during the process from uncontrolled to stable blowing control are given in Figure 9 for the state of 30° flaps and a 10° angle of attack. In natural conditions, the cross-flow developed at the flaps moves in the direction of the wing tip, and there is a clear separation between the flaps and the wing tip surface. As combined control is applied, the tip separation is first restrained and the separation gradually moves in the direction of the flow, with the cross-flow being impeded by the blowing and gradually decreasing in distance along the span. As the injection momentum is further increased, no significant cross-flow occurs, and the combined blowing effectively suppresses flow separation.

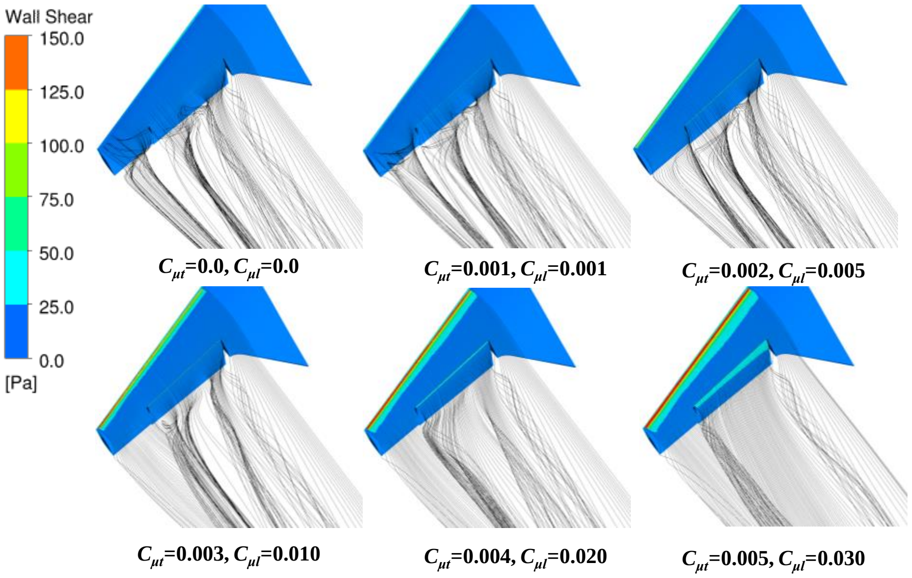

$C_{\mu t}$=0.0, $C_{\mu l}$=0.0 $C_{\mu t}$=0.001, $C_{\mu l}$=0.001 $C_{\mu t}$=0.002, $C_{\mu l}$=0.005

$C_{\mu t}$=0.003, $C_{\mu l}$=0.010 $C_{\mu t}$=0.004, $C_{\mu l}$=0.020 $C_{\mu t}$=0.005, $C_{\mu l}$=0.030

Figure 9. Wall shear and streamlines at different momentum coefficients.

Figure 10 shows the lift coefficient results at different moments for a flap angle of 30° and 10° attack of angle, where the combined blowing starts at the moment t = 100 ms and the momentum coefficient gradually becomes steady around 0.03 and 0.005 after the moment t = 300 ms. Around t = 200 ms, there is a tendency for the lift coefficient to decrease and then increase, consistent with previous research [29]; however, this phenomenon is not analyzed with respect to the flow field. The lift coefficient gradually stabilizes after approximately 200 ms, when the momentum of the combined blowing injection stabilizes. In order to identify the reasons for variations in the lift coefficients, an analysis of the evolution process of the flow field resulting from combined blowing excitation was conducted.

Figure 11 shows the time-dependent induced flow field in a typical chordal cross-section after using combined blowing. Before t = 200 ms, a significant low-speed separation is evident on the upper surface of the flap, and the flow line depicts the separation vortex gradually moving downstream with time. At t = 200 ms, the separation region is squeezed by the injection, and this leads to a slight increase in the separation compared to the period before, which may be the reason for the decrease in the lift coefficient. When t = 300 ms, the effect of combined blowing becomes pronounced, and the low-speed separation region is flattened and concentrated near the TE of the flap. At t = 400 ms, separation is effectively restrained, and the high-speed region on the suction surface of the wing spreads in the flow direction from the leading edge. When t = 500 ms, the induced flow field stabilizes, and the induced injection velocity exhibits minimal variation over time.

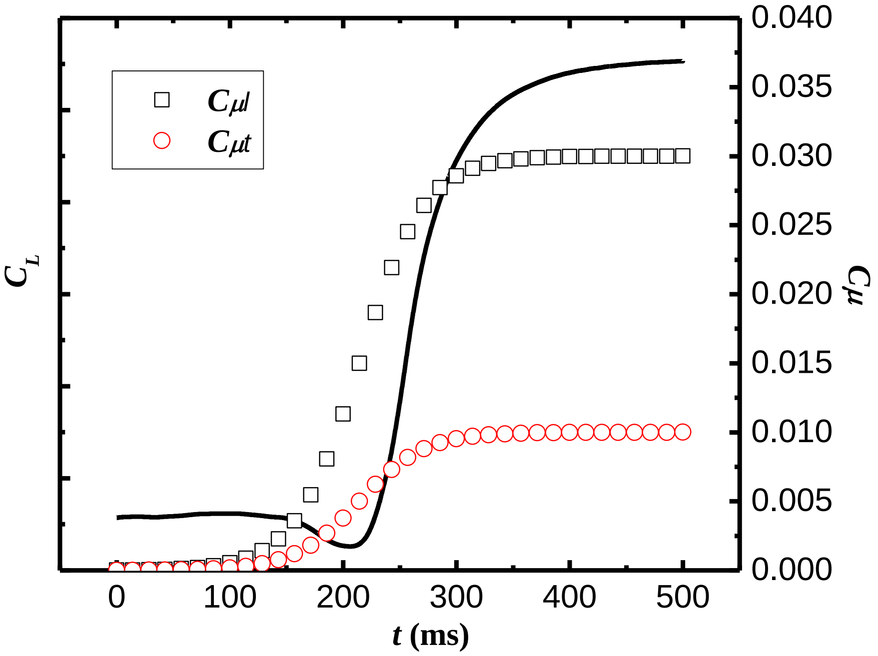

Figure 10. Lift coefficient variation curve during combined blowing control.

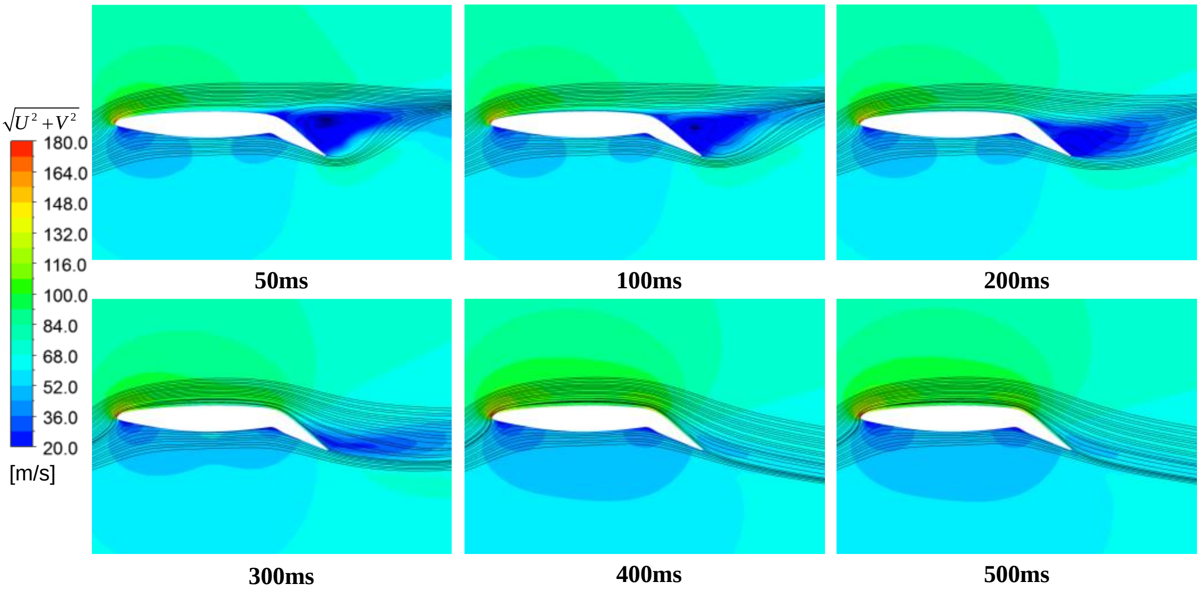

Figure 11. Combined-blowing-induced flow field change process.

Figure 12 shows the variation in the transient vortex field in a typical spanwise cross-section of the aircraft. At t = 200 ms, the vortex break-up causes a number of vortices with different directions and a low strength. As the combined blowing momentum coefficient gradually increases and stabilizes, the low-intensity vortices gradually disappear. After t = 400 ms, the injected momentum significantly enhances the vortex strength and delays the vortex break-up, which, in turn, enhances its stability and induces the stabilization of the flow field.

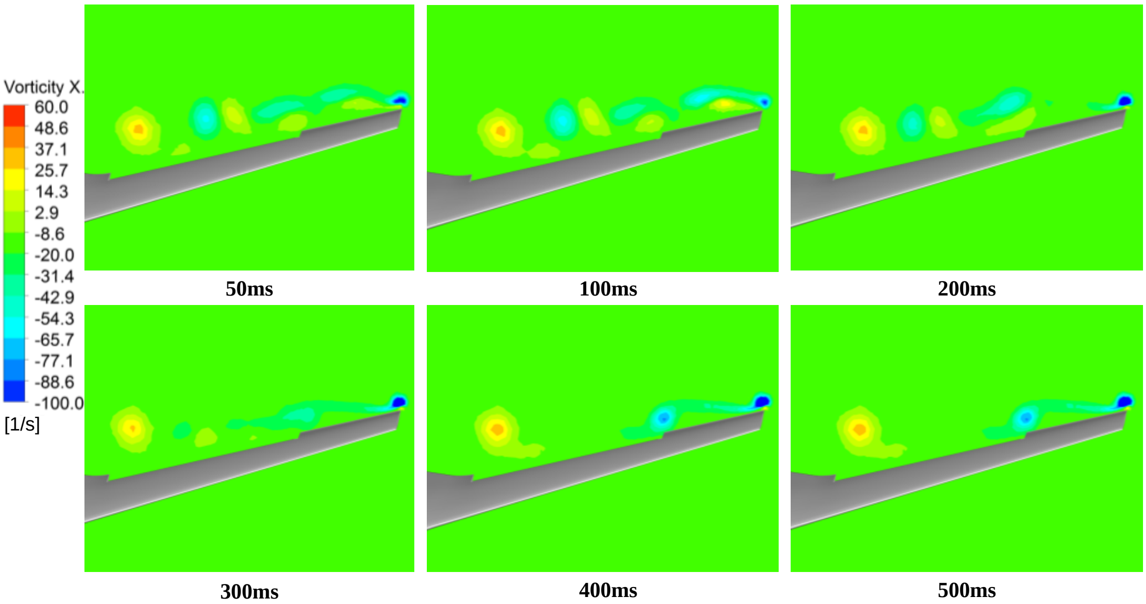

Figure 12. Combined-blowing-induced flow field vortices' change process.

3.5. Surface Pressure and Velocity Distribution

To compare the pressure changes on the aircraft surface with and without control and to provide a reference for the adhesive position of the thread in the flow visualization test, the pressure coefficients and Mach number clouds for different spanwise profiles of the wing without control and combined blowing control are provided in Figures 13 and 14. Combining the results of these figures at an angle of attack of 10°, there is separation at the wing tip in natural conditions, the suction peak at the wing tip is weakened, and the flow velocity in the flap and wing tip region is lower. When combined blowing control is applied, the injection weakens the effect of the cross-flow and, thus, the buildup of the boundary layer at the wing tip, and the pressure gradient distribution in the flow direction is restored. Moreover, the range of the low-speed region is significantly reduced after the injection of momentum, and the slope of the lift line remains basically the same before and after combined blowing control is applied (see Figure 7). Based on these results, the density of the visual slit slightly increased to an appropriate degree at the TE, LE, and wingtip locations.

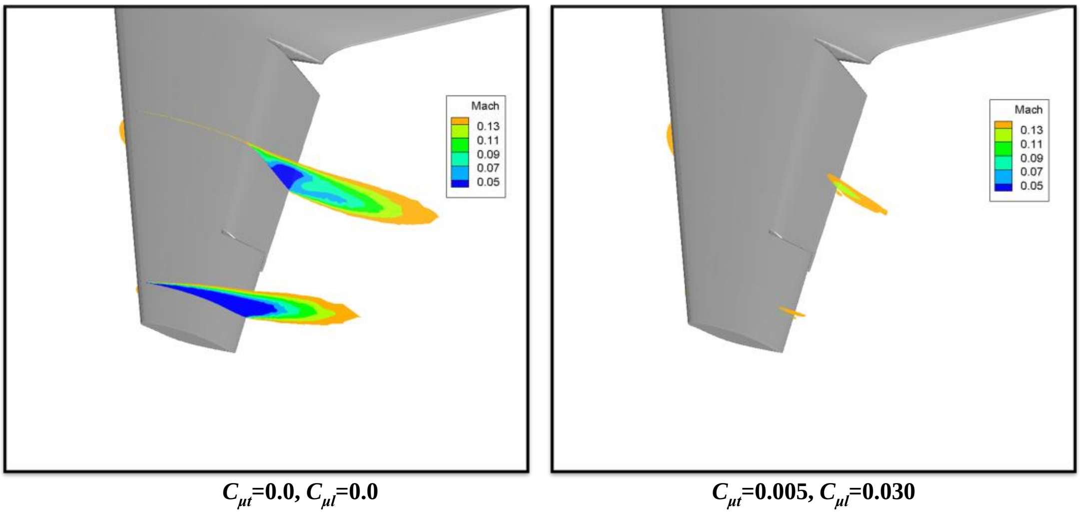

$C_{\mu t}$=0.0, $C_{\mu l}$=0.0 $C_{\mu t}$=0.005, $C_{\mu l}$=0.030

Figure 13. Mach number contours for different spanwise profiles of the wing (Y/Span = 60%, 90%).

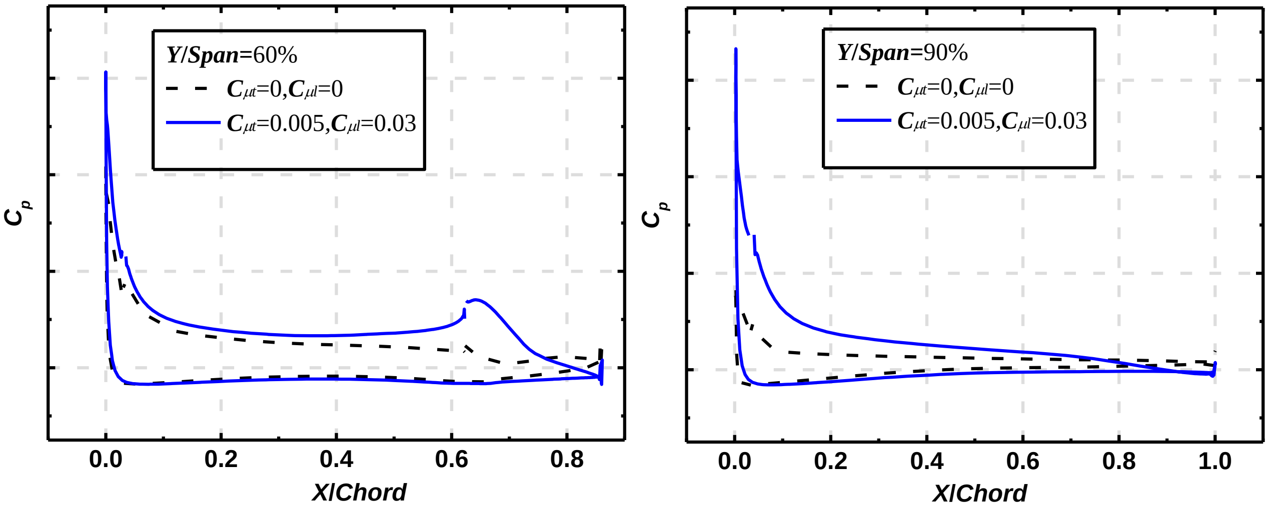

Figure 14. Pressure coefficients for different spanwise profiles of the wing.

4. Test Results and Discussion

4.1. Data Repeatability

Under the condition of a wind speed of 50 m/s (Reynolds number 1.75 × 10^6), seven repeatability verification tests were conducted. Table 1 shows the maximum mean square deviation of the seven repeatability test results.

Table 1. Repeatability test data.

$\alpha/°$	σ_{CL}	σ_{CD}	σ_{Cm}
−4	0.001260	0.000286	0.000426
−2	0.001170	0.000320	0.000538
0	0.000899	0.000354	0.000442
2	0.000839	0.000348	0.000320
4	0.000940	0.000313	0.000492
6	0.000746	0.000324	0.000527
8	0.000936	0.000346	0.000522
10	0.000761	0.000430	0.000353

The mean square deviation is the square root of the ratio of the sum of the squares for the deviations of the test values x from the average value μ to the number of observations N. It is defined here in Equation (3) as:

$$\sigma_{SD} = \sqrt{\frac{1}{N}\sum_{i=1}^{N}\left(x^{(i)} - \mu\right)^2} \quad (3)$$

The maximum mean square deviations of the lift and drag coefficients do not exceed 0.002 and 0.0005, respectively, and this accuracy meets the wind tunnel test specification.

4.2. Uncontrolled Performance

Figure 15 shows the test model's lift and drag coefficient curves for different flap deflections at a wind speed of 50 m/s. The lift coefficient of the HWB with flap angles of 30° and 60° increased by approximately 0.223 and 0.382, respectively, compared to the cruise configuration (α = 8°). With the increase in the flap angle, the separation vortex on the suction surface of the flap gradually increased, resulting in a lack of increase in the lift with the enhancement of the curvature, while the drag coefficient increased significantly. Compared to the cruise configuration, the stall angle was increased by approximately 2° at the flap angle of 30° and by approximately 4° at the flap angles of 40° and 60°. Similar to the conclusion in [18], the lift enhancement effect of the seamless, simple flap is limited and causes a forward stall angle, accompanied by higher drag, which requires a combination of flow control methods to further improve the lift.

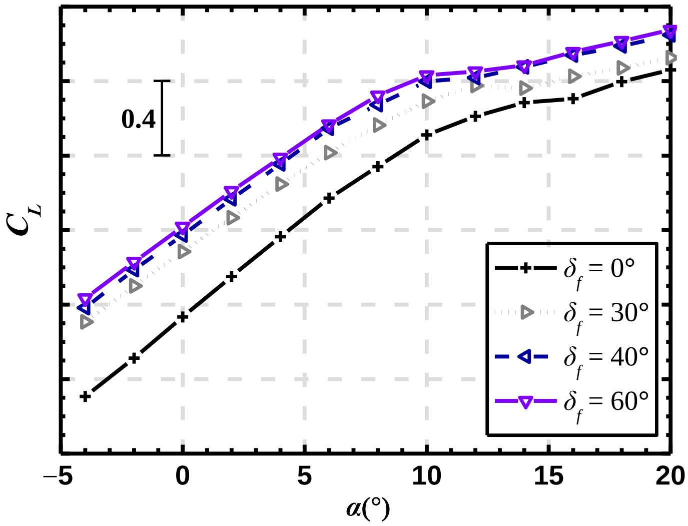

(**a**)

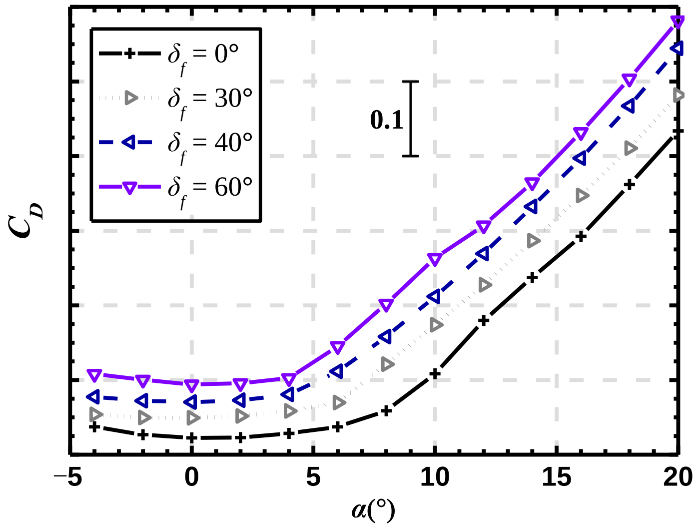

(**b**)

Figure 15. Basic aerodynamic performance with variable flap skewness: (**a**) $C_L \sim \alpha$; (**b**) $C_D \sim \alpha$.

In Figure 16, when the angle of attack is 4° and the flap angle is 60°, the suction surface of the flap is completely separated due to the lack of effective slit flow. The separated region on the main wing is mainly concentrated in the area near the LE covering 1/3 of the wing root and the middle section when the angle of attack is 8°. With the increase in the angle of attack, the reverse pressure gradient is further enhanced, resulting in the expansion of the separation on the main wing from the LE to the entire outer wing section, with a strong separation forming in the middle section. As shown in Figure 15, separation reduces the slope of the lift linear segment and increases the drag.

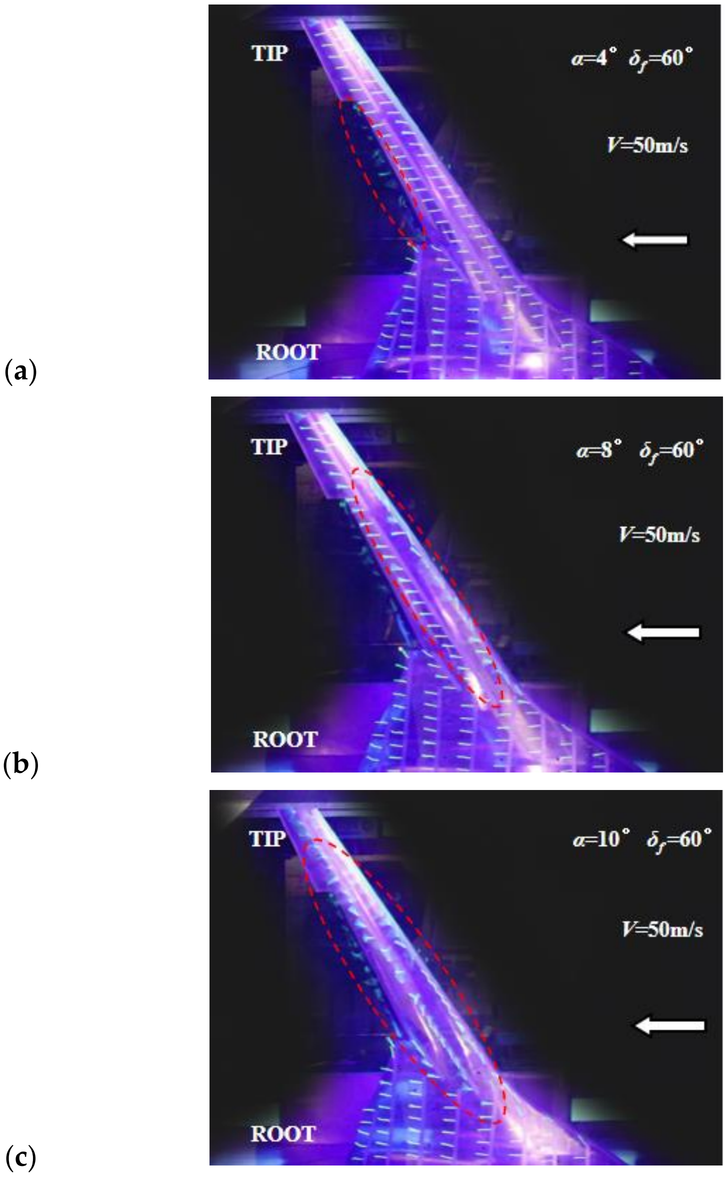

Figure 16. Flow visualization on suction side (uncontrolled, arrows indicate the direction of incoming flow): (**a**) α = 4°; (**b**) α = 8°; (**c**) α = 10°.

In contrast, the 30° flap angle has a significant lift enhancement effect, a larger stall angle of attack, and a smaller drag coefficient; thus, the following section focuses on the study of blowing lift enhancement technology based on a 30° flap angle.

4.3. Effect of TE Blowing Alone

With no incoming wind and a 30° flap angle, the additional force and moments caused by different TE blowing momentum coefficients are shown in Figure 17. When the momentum coefficient is a relatively large, at 0.04, the additional lift, drag, and pitch moment loads are 1.7%, 3.8%, and 3.7%, respectively, compared to aerodynamic loads when there is a wind speed of 50 m/s. Since the changes in the aerodynamic coefficients caused by the additional loads are relatively small and also affect the actual flight state, the following test results are not deduced from the additional force and moments.

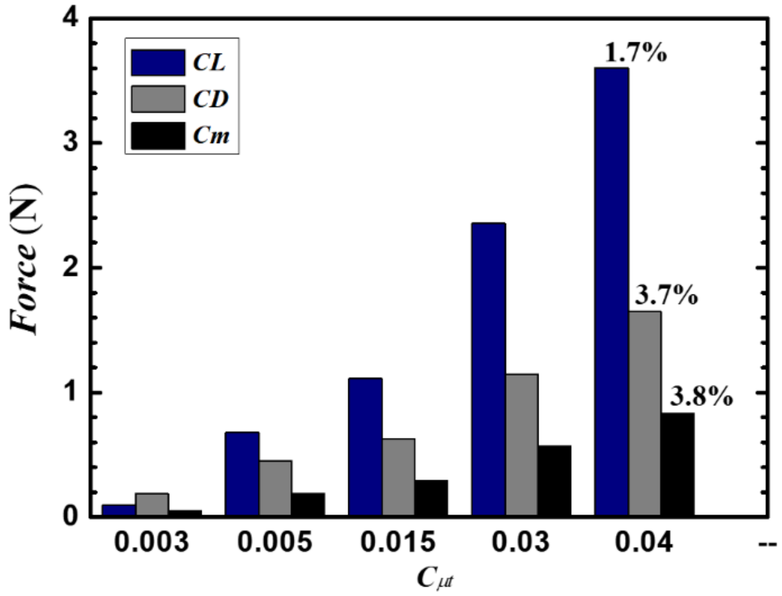

Figure 17. Influence of blowing control on force or moment measurement results.

When the wind speed is 50 m/s and the flap angle is 30°, the lift and drag coefficients of different TE blowing momentum coefficients change with the angle of attack, as presented in Figure 18. With the increase in the momentum coefficient, the linear section lift gradually increases, and the linear lift enhancement effect at the uncontrolled 40° flap angle is reached when the momentum coefficient is 0.005. The momentum coefficient of 0.015 increases the lift by approximately 0.215 (α = 4°). At the same time, over the entire range of the test angle of attack, the drag coefficient with TE blowing is approximately 0.02, smaller than that under an uncontrolled 40° flap. The lift–drag ratio of the small flap angle with TE blowing is significantly higher than that of the uncontrolled large flap angle, but with the increase in the angle of attack, the lift–drag ratio of the two states tends to be consistent (see Table 2).

Table 2. Comparison of lift–drag ratio between TE blowing and uncontrolled state.

α/°	***L/D***		**$\Delta L/D$**	**$\frac{\Delta L/D}{(L/D)_{\delta_f=40°}}$**
	δ_f = 30° ($C_{\mu t}$ = 0.015)	**δ_f = 40° (Uncontrolled)**		
4	12.908	9.342	3.566	38.2%
6	11.124	8.472	2.651	31.3%
8	8.368	6.791	1.577	23.2%
10	6.512	5.659	0.853	15.1%
12	5.169	4.526	0.643	14.2%
14	4.146	3.837	0.310	8.1%

In summary, TE blowing alone can significantly enhance the linear section of the lift and provide a significant lift-to-drag ratio advantage over the uncontrolled large flap deflection state prior to stall. However, as the blowing momentum coefficient increases, the stall gradually advances.

A significant flap suction surface separation occurs at a wind speed of 50 m/s and an angle of 4° with no control applied. A TE blowing momentum coefficient of 0.005 at a 4° angle of attack alone can restrain flap separation (see Figure 19).

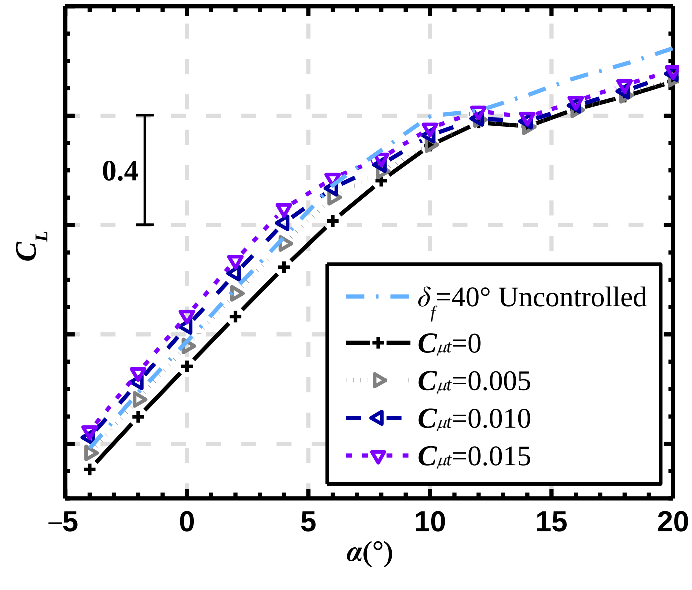

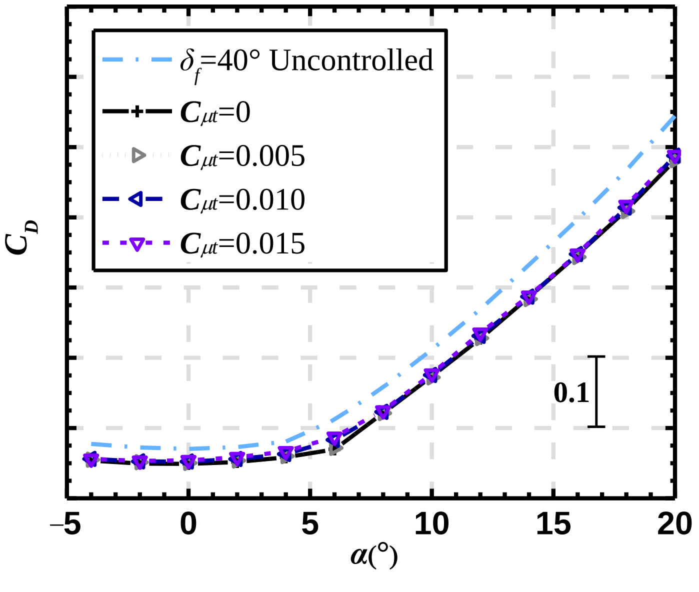

Figure 18. Lift and drag coefficient curves for different momentum coefficients (δ_f = 30°): (**a**) C_L~α; (**b**) C_D~α.

In addition, with a flap deflection of 30° and a 6° angle of approach, without blowing control, there is a significant separation on both the flap and the main wing suction surfaces, as shown in Figure 19c, with the spanwise flow starting at the transition between the wing and the fuselage (see the solid yellow line) and significant backflow at the LE (see the dashed red line). This indicates that although TE blowing can effectively suppress flap airflow separation, there is still a significant separation at the LE. Thus, further research is needed to investigate the effect of blowing control near the LE on lift performance.

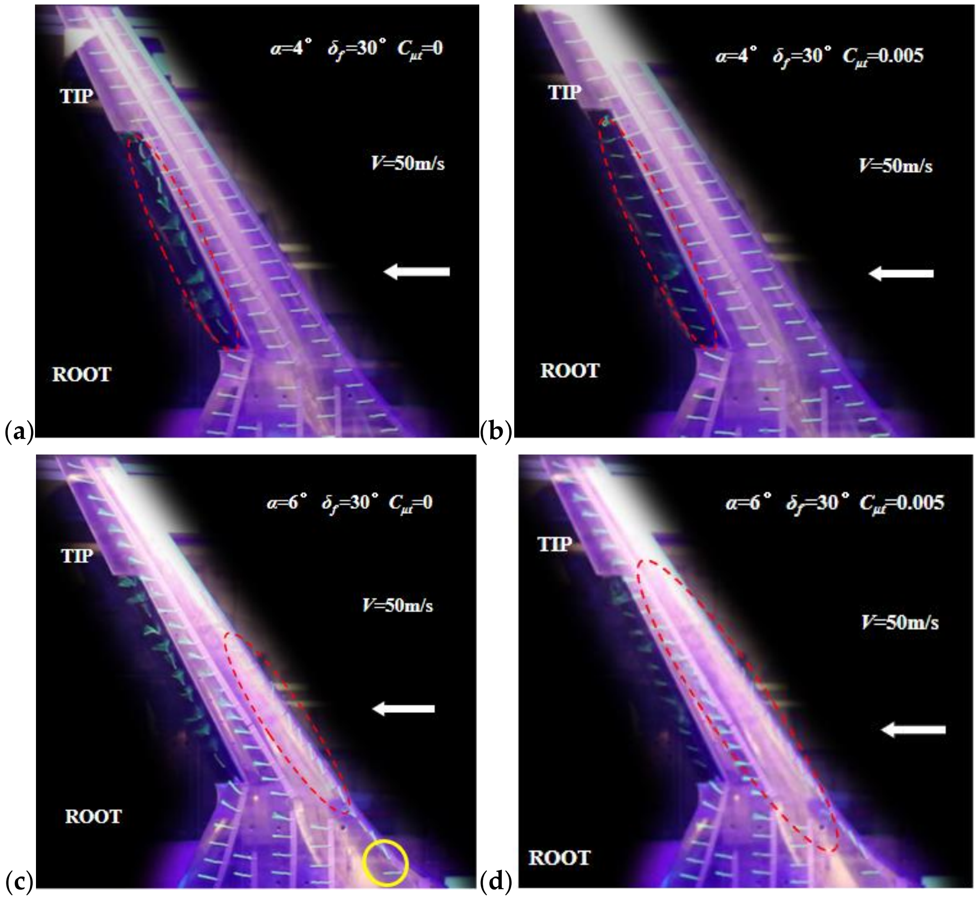

Figure 19. Flow visualization using silk on the suction side (TE blowing alone, arrows indicate the direction of incoming flow): (**a**) α = 4°, $C_{\mu t}$ = 0; (**b**) α = 4°, $C_{\mu t}$ = 0.005; (**c**) α = 6°, $C_{\mu t}$ = 0; (**d**) α = 6°, $C_{\mu t}$ = 0.005.

4.4. Effect of LE Blowing Alone

Figure 20 shows the characteristic lift curves of the model after applying LE blowing control alone at a flap deflection angle of 30°. The lift linear segment did not change significantly compared with the uncontrolled state. However, the stall delay effect was significant, with a maximum increase in the lift coefficient of approximately 0.16 (α = 16°) and an increase in the stall angle from 12° to 18°.

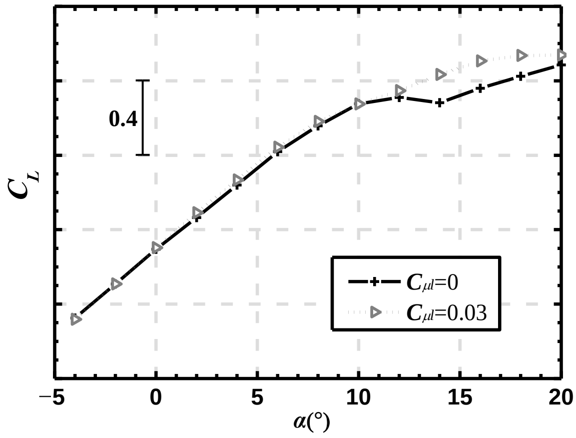

Figure 20. Lift coefficient curves for LE blowing control and uncontrolled state (δ_f = 30°).

In summary, the effect of TE blowing alone on the aerodynamic characteristics of the model is mainly observed before the stall, while the effect of LE blowing alone on the lift is mainly observed after the stall. Therefore, blowing at the leading and trailing edges of the main wing can be used for flow control to achieve an increased lift linear segment while delaying stall.

4.5. Combined Blowing Control

Whether the injection is supplied using engine-induced air or other equipment, the achievement of maximum lift enhancement at a minimal energy cost is expected. When the wind speed is 50 m/s and the flap deflection angle is 30°, blowing control is applied simultaneously to both the leading and trailing edges of the main wing. Combining the results in Figure 18a, TE blowing uses a relatively small momentum coefficient of 0.005 to ensure that the leading edge has enough momentum to suppress the larger separation region of the main wing suction surface.

The resulting lift and drag coefficient curves are shown in Figure 21. The lift linear segment during combined blowing and TE blowing alone is basically the same, and after the angle of attack of 6°, the combined blowing significantly delays the stall, with a maximum lift enhancement of approximately 0.19 ($\alpha = 14°$). The lift linear segment under combined blowing reaches the effect of gain in the 40° flap uncontrolled state, and after the angle of attack of 10°, the combined blowing continues to increase the lift coefficient. As shown in Figure 21b, the drag reduction at an angle of attack of 8° is approximately 0.024, which is approximately 0.06 lower than the drag coefficient at 40° flaps without control.

Table 3 shows the lift-to-drag ratios for 30° flaps with combined blowing control and 40° flaps without control. Compared to the larger uncontrolled flap deflection state, the smaller flap deflection state with control applied maintains a specific advantage in the 4° to 12° angle of attack range due to the delayed stall effect of combined blowing, with increments of 2.2 or more.

Table 3. Comparison of lift–drag ratio between combined blowing and uncontrolled state.

	L/D			
α/°	**$\delta_f = 30°$ ($C_{\mu t} = 0.005$ $C_{lt} = 0.030$)**	**$\delta_f = 40°$ (Uncontrolled)**	**$\Delta L/D$**	**$\frac{\Delta L/D}{(L/D)_{\delta_f=40°}}$**
4	13.110	9.342	3.768	40.3%
6	13.107	8.472	4.635	54.7%
8	11.148	6.790	4.357	64.2%
10	9.016	5.659	3.357	59.3%
12	6.777	4.526	2.251	49.7%
14	5.240	3.837	1.403	36.6%

The separation of the flap is effectively suppressed when TE blowing control is used with $C_{\mu t} = 0.005$, but the separation area of the main wing suction surface is extensive, and stall occurs, as can be seen in Figure 22a. For $C_{\mu t} = 0.015$ and $C_{\mu l} = 0.03$, except for a slight separation at the unarranged blown slot at the wing root, no significant separation is observed between the wing tip and the middle section of the main wing, effectively delaying stall.

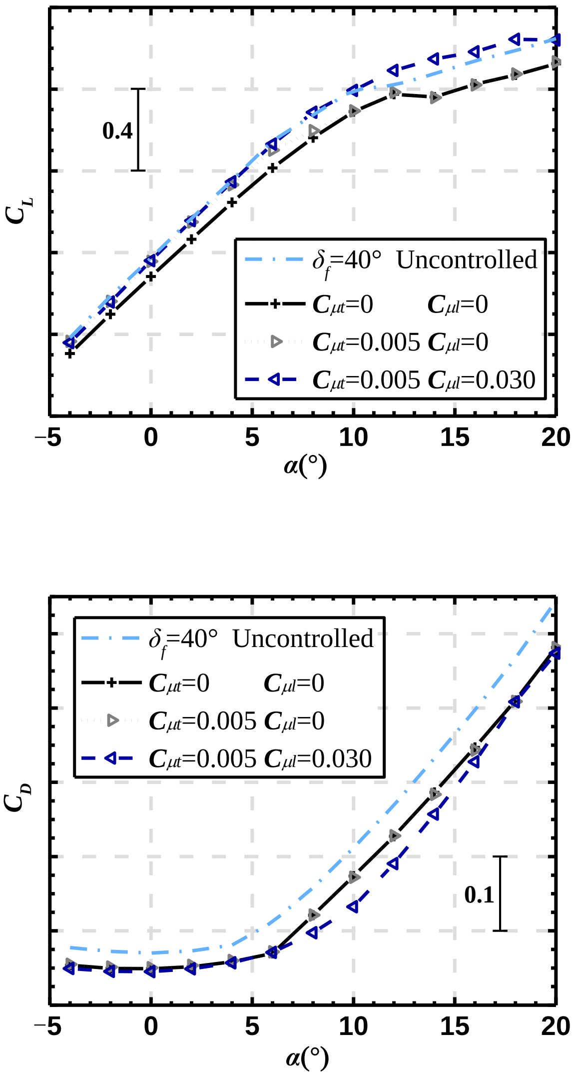

(**a**)

(**b**)

Figure 21. Lift coefficient curve based on combined blowing (δ_f = 30°): (**a**) C_L~α; (**b**) C_D~α.

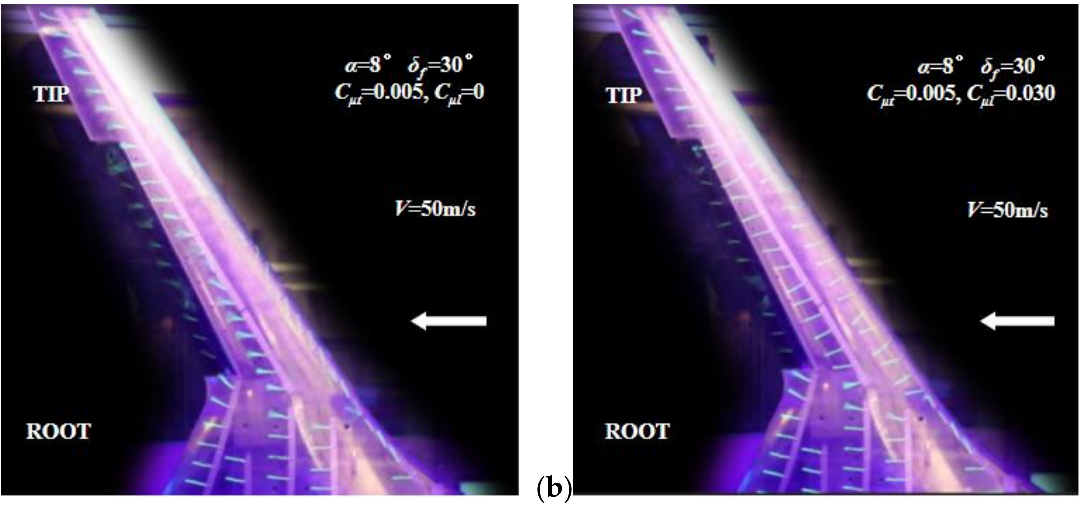

(**a**) (**b**)

Figure 22. Flow visualization using silk on the suction side (combined blowing, arrows indicate the direction of incoming flow): (**a**) $C_{\mu t}$ = 0.005, $C_{\mu l}$ = 0; (**b**) $C_{\mu t}$ = 0.005, $C_{\mu l}$ = 0.030.

5. Conclusions

In this paper, the CFD method was used to analyze the combined jet control mechanism for the HWB aircraft. Through wind tunnel tests, the investigation first analyzed a seamless flap without an exposed structure for HWB applications. Then, the control effects of TE and LE blowing were investigated separately. Finally, a more efficient combined blowing flow control method was proposed. The results show that:

The combination of blowing prevents the development of cross-flow and weakens the accretion of the boundary layer at the wing tips. The injection of momentum delays vortex break-up, and the combination of blowing effectively restrains flow separation.

Seamless, simple flaps have a limited effect on lift enhancement. The premature separation of the flap suction surfaces leads to earlier stalls and must be combined with blowing control to exploit the increasing lift capability.

The effect of the blown deflected TE method on the model's aerodynamic characteristics is mainly observed before the stall. In contrast, the blown LE method mainly increases the lift after the stall.

The combined blowing technique increases the lift in the linear section while delaying the stall angle. The maximum lift increment is approximately 0.19, and the stall angle of attack is increased from 12° to 18°, with a drag reduction effect. The controlled flap deflection of 30° yields an increase in the lift-to-drag ratio of more than 2.2 compared to the uncontrolled flap deflection of 40° in an angle of attack range of 4° to 12°.

Author Contributions: Conceptualization, J.P. and W.W.; methodology, J.P.; software, W.W.; data curation, J.P.; formal analysis, C.Q.; writing—original draft preparation, J.P.; writing—review and editing, Q.S.; supervision, X.W. and X.Z.; project administration, W.W.; funding acquisition, W.W. All authors have read and agreed to the published version of the manuscript.

Funding: This research received no external funding.

Data Availability Statement: Not applicable.

Conflicts of Interest: The authors declare no conflict of interest.

References

1. Liebeck, R.H. Design of the Blended Wing Body Subsonic Transport. *J. Aircr.* **2004**, *41*, 10–25. [CrossRef]
2. Panagiotou, P.; Antoniou, S.; Yakinthos, K. Cant angle morphing winglets investigation for the enhancement of the aerodynamic, stability and performance characteristics of a tactical Blended-Wing-Body UAV. *Aerosp. Sci. Technol.* **2022**, *123*, 107467. [CrossRef]
3. Larkin, G.; Coates, W. A design analysis of vertical stabilisers for Blended Wing Body aircraft. *Aerosp. Sci. Technol.* **2017**, *61*, 51–61. [CrossRef]
4. Graham, W.R.; Hall, C.A.; Morales, M.V. The potential of future aircraft technology for noise and pollutant emissions reduction. *Transp. Policy* **2014**, *34*, 36–51. [CrossRef]
5. Ammar, S.; Legros, C.; Trépanier, J.Y. Conceptual design, performance and stability analysis of a 200 passengers Blended Wing Body aircraft. *Aerosp. Sci. Technol.* **2017**, *65*, S1270963816312640. [CrossRef]
6. Xin, Z.; Chen, Z.; Gu, W.; Zhang, M.; Zhang, B. Externally blown elevon applied for the longitudinal control of blended wing body transport with podded engines. *Aerosp. Sci. Technol.* **2019**, *93*, 105324. [CrossRef]
7. Hooker, J.R. Design of a Hybrid Wing Body for Fuel Efficient Air Mobility Operations at Transonic Flight Conditions. In Proceedings of the 52nd Aerospace Sciences Meeting, National Harbor, MD, USA, 13–17 January 2014; American Institute of Aeronautics and Astronautics: Reston, VA, USA, 2014.
8. Wick, A.T.; Hooker, J.R.; Walker, J.; Chan, D.T.; Plumley, R.; Zeune, C. *Hybrid Wing Body Performance Validation at the National Transonic Facility*; NASA Technical Report AIAA-2017-0099; American Institute of Aeronautics and Astronautics: Reston, VA, USA, 2017.
9. Peter, M.; Shmilovich, A.; Douglas, S. *Refined AFC-Enabled High-Lift System Integration Study*; NASA Technical Report NASA/CR–2016-219170; National Aeronautics and Space Administration: Hampton, VA, USA, 2016.
10. McLean, J.; Crouch, J.; Stoner, R.; Sakurai, S.; Seidel, G.E.; Feifel, W.M.; Rush, H.M. *Study of the Application of Separation Control by Unsteady Excitation to Civil Transport Aircraft*; NASA Technical Report NASA-CR-1999-209338; American Institute of Aeronautics and Astronautics: Reston, VA, USA, 1999.
11. Smith, D.; Dickey, E.; Vonklein, T. The ADVINT Program. In Proceedings of the 3rd AIAA Flow Control Conference, San Francisco, CA, USA, 5–8 June 2006.
12. Bumazzi, M.; Radespiel, R. Design and Analysis of a Droop Nose for Coanda Flap Applications. *J. Aircr.* **2014**, *51*, 1567–1579.

13. Radespiel, R.; Burnazzi, M. *Active Flow and Combustion Control*; Springer: Berlin, Germany, 2015; pp. 101–114.
14. Rao, R. Acquisition of Japanese Aircraft likely in 2015. *Int. Aerosp. Rev. Anal.* **2015**, *17*, 41.
15. Lichtwardt, J.; Paciano, E.; Marshall, D.; Jameson, K.K. STOL Performance of Cal Poly's AMELIA. In Proceedings of the 2013 AIAA Atmospheric Flight Mechanics Conference, Grapevine, TX, USA, 7–10 January 2013; American Institute of Aeronautics and Astronautics: Reston, VA, USA, 2013.
16. Collins, S.W.; Westra, B.W. Wind Tunnel Testing of Powered Lift, All-Wing STOL Model. *Aeronaut. J.* **2009**, *113*, 323–331. [CrossRef]
17. Milholen, W.; Jones, G.; Cagle, C. NASA high Reynolds number circulation control research-overview of CFD and planned experiments. In Proceedings of the AIAA Aerospace Sciences Meeting, Orlando, FL, USA, 4–7 January 2010; American Institute of Aeronautics and Astronautics: Reston, VA, USA, 2010.
18. Lin, J.C.; Melton, L.; Hannon, J.; Andino, M.Y.; Koklu, M.; Paschal, K.C.; Vatsa, V.N. Wind Tunnel Testing of High Efficiency Low Power (HELP) Actuation for Active Flow Control. In Proceedings of the AIAA Scitech 2020 Forum, Orlando, FL, USA, 6–10 January 2010; American Institute of Aeronautics and Astronautics: Reston, VA, USA, 2020.
19. Imamura, T.; Ura, H.; Yokokawa, Y.; Yamamoto, K. *A Far-Field Noise and Near-Field Unsteadiness of a Simplified High-Lift-Configuration Model(Slat)*; AIAA Paper, no. 1239; American Institute of Aeronautics and Astronautics: Reston, VA, USA, 2009.
20. Jameson, K. Part 1: The Wind Tunnel Model Design and Fabrication of Cal Poly's AMELIA 10 Foot Span Hybrid Wing-Body Low Noise CESTOL Aircraft. In Proceedings of the AIAA Atmospheric Flight Mechanics Conference, Portland, OR, USA, 8–11 August 2011; American Institute of Aeronautics and Astronautics: Reston, VA, USA, 2011.
21. Hooker, J.R.; Wick, A.T.; Hardin, C.J. *Commercial Cargo Derivative Study of the Advanced Hybrid Wing Body Configuration with Over-Wing Engine Nacelles*; NASA Technical Report NASA/CR-2017-219653; National Aeronautics and Space Administration: Hampton, VA, USA, 2017.
22. Chan, D.T.; Hooker, J.R.; Wick, A.; Plumley, R.W.; Zeune, C.H.; Ol, M.V.; DeMoss, J.A. Transonic Semispan Aerodynamic Testing of the Hybrid Wing Body with Over Wing Nacelles in the National Transonic Facility. In Proceedings of the 55th AIAA Aerospace Sciences Meeting, Grapevine, TX, USA, 9–13 January 2017; American Institute of Aeronautics and Astronautics: Reston, VA, USA, 2017.
23. Galbtaith, M.C. Numerical simulations of a high-lift airfoil employing active flow control. In Proceedings of the 44th AIAA Aerospace Sciences Meeting and Exhibit, Reno, NV, USA, 9–12 January 2006.
24. Shmilovich, A.; Yadlin, Y. Flow control for the systematic buildup of high-lift systems. *J. Aircr.* **2008**, *45*, 1680–1688. [CrossRef]
25. Bauer, M.; Peltzer, I.; Nitsche, W.; Gölling, B. *Active Flow Control on an Industry-Relevant Civil Aircraft Half Model*; Springer: Berlin, Germany, 2010.
26. Chen, J.; Wu, X.; Zhang, J.; Li, B.; Jia, H.; Zhou, N. FlowStar: General unstructured-grid CFD software for National Numerical Wind tunnel (NNW) Project. *Acta Aeronaut. Astronaut. Sin.* **2021**, *42*, 9–30.
27. Roe, P.L. Approximate Riemann solvers, parameter vectors, and difference schemes. *J. Comput. Phys.* **1981**, *43*, 357–372. [CrossRef]
28. Wick, A.T.; Hooker, J.R.; Clark, C.M. Powered Low Speed Testing of the Hybrid Wing Body. In Proceedings of the 55th AIAA Aerospace Sciences Meeting, Grapevine, TX, USA, 9–13 January 2017.
29. Chen, C.; Zakharin, B.; Wygnanski, I.J. On the parameters governing fluidic control of separation and circulation. In Proceedings of the 46th AIAA Aerospace Sciences Meeting and Exhibit, Reno, NV, USA, 7–10 January 2008.

Disclaimer/Publisher's Note: The statements, opinions and data contained in all publications are solely those of the individual author(s) and contributor(s) and not of MDPI and/or the editor(s). MDPI and/or the editor(s) disclaim responsibility for any injury to people or property resulting from any ideas, methods, instructions or products referred to in the content.